# Green Chemistry

Cutting-edge research for a greener sustainable future
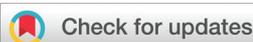
ROYAL SOCIETY
OF **CHEMISTRY**

**PAPER**
Qian Chen, Amanda J. Hughes *et al.*
Ambient and green processing of lead-free double
perovskite Cs₂AgBiBr₆ films

25 YEARS
ANNIVERSARY

## PAPER

Check for updates

# Ambient and green processing of lead-free double perovskite Cs$_2$AgBiBr$_6$ films†

Qian Chen, ✱[a] Abhinav K. Singh, [a,b] Hissah Alghathami, [a,b] Xuzhao Liu,[c,d] Kun Huang,[e] Andrew G. Thomas,[c,d] Richard J. Curry, [d,f] Laurie J. Phillips [b] and Amanda J. Hughes ✱[a]

Lead-free inorganic perovskite Cs$_2$AgBiBr$_6$ has emerged as a promising alternative to lead-based halide perovskites (LHPs), addressing concerns over toxicity and stability. However, fabricating high-quality Cs$_2$AgBiBr$_6$ films remains significantly more challenging than LHPs. Here, we investigate the impact of processing environments on film morphology, comparing deposition in ambient air and under a nitrogen environment. We find that moisture levels play a critical role in determining Cs$_2$AgBiBr$_6$ film quality, with significant differences observed between the controlled glovebox environment (~1 ppm moisture) and ambient air with a relative humidity of 60–70%. Pristine films processed in ambient air show large aggregates and poor surface coverage, whereas dense and uniform films are achieved in a nitrogen glovebox. However, achieving cost-effective and scalable manufacturing requires ambient processing methods. To overcome this challenge, we introduce an ethyl acetate (EA) antisolvent treatment that enables the ambient deposition of dense and uniform Cs$_2$AgBiBr$_6$ films, even at a high relative humidity (60–70%). This approach enhances film morphology, crystallinity, and device performance, leading to a five-fold improvement in power conversion efficiency (PCE). EA-treated films achieving a PCE of 1.08%, compared to 0.21% for pristine films are reported. Recognizing the importance of solvent toxicity in ambient and scalable production, we assess the environmental impact using the CHEM21 framework, finding both the precursor solvent and antisolvent in this work to be environmentally favorable. Our findings offer a green, simple, and ambient fabrication strategy for high-quality, lead-free Cs$_2$AgBiBr$_6$ films, advancing their potential for future optoelectronic applications such as solar cells, photodetectors, and memristors.

### Green foundation

1. This work introduces a green and cost-effective method for processing high-quality lead-free perovskite Cs$_2$AgBiBr$_6$ films under ambient conditions, reducing dependence on harmful solvents and energy-intensive nitrogen environment.

2. Using the CHEM21 framework, we confirm the environmental favorability of ethyl acetate (EA) as the antisolvent and dimethyl sulfoxide (DMSO) as the precursor solvent used in this work. The EA antisolvent treatment enables the formation of dense and uniform Cs$_2$AgBiBr$_6$ films even under a high relative humidity condition (60–70%), resulting in a fivefold improvement in device power conversion efficiency (PCE)—from 0.21% for pristine films to 1.08% for EA-treated films.

3. Further research will focus on adapting this method for scalable manufacturing, such as antisolvent bathing to enhance scalability, sustainability, and industrial viability.

*$^a$Department of Materials, Design & Manufacturing Engineering, School of Engineering, University of Liverpool, UK. E-mail: qian.chen@liverpool.ac.uk, amanda.hughes2@liverpool.ac.uk*
*$^b$Stephenson Institute for Renewable Energy, Department of Physics, University of Liverpool, Liverpool, L69 7ZF, UK*
*$^c$Department of Materials, School of Natural Science, The University of Manchester, Oxford Road, Manchester M13 9PL, UK*

*$^d$Department of Electrical and Electronic Engineering, Photon Science Institute, University of Manchester, Manchester, M13 9PL, UK*
*$^e$National Graphene Institute & Department of Chemical Engineering, University of Manchester, Manchester, M13 9PL, UK*
*$^f$Department of Electrical and Electronic Engineering, University of Manchester, Manchester M13 9PL, UK*
†Electronic supplementary information (ESI) available. See DOI: https://doi.org/10.1039/d5gc00722d

# 1. Introduction

Lead-based halide perovskites (LHPs) have attracted significant attention over the past decade due to their outstanding intrinsic properties, including adjustable bandgap, high absorption coefficient, long charge-carrier lifetime, and strong defect tolerance.[1,2] These remarkable optoelectronic characteristics have positioned LHP as a promising material for diverse applications such as solar cells, photodetectors, X-ray detectors, photocatalysis, solar concentrators, and light-emitting diodes.[3,4] Notably, LHP solar cells have achieved a record power conversion efficiency (PCE) of 26.7%.[5] Despite their potential, the toxicity of water-soluble lead compounds in LHP raises serious concerns for human health and the environment.[6] Research suggests that lead leakage from LHP solar cells poses a significant environmental hazard, as research shows that lead from LHP solar cells is more easily absorbed by plants compared to other sources of lead contamination, ultimately entering the food chain.[7] If encapsulation fails, rainwater can accelerate lead leaching, threatening both human health and ecosystems. Furthermore, studies indicate that end-of-life LHP solar cells should be treated as hazardous waste rather than disposed of in landfills, which substantially increases life-cycle costs.[8]

Additionally, conventional LHP fabrication relies on toxic or hazardous solvents such as N,N-dimethylformamide (DMF), N-methylpyrrolidone (NMP), chlorobenzene (CB), toluene, and diethyl either further increasing potential health and environmental concerns.[9] Given these risks, raising awareness of these challenges while actively pursuing safer alternatives is crucial. The development of lead-free perovskites with green processing methods is essential for ensuring both environmental sustainability and human safety. Furthermore, LHPs are susceptible to moisture- and oxygen-induced degradation, particularly under photoexcitation and high-temperature conditions, presenting significant barriers to their commercialization.[2] Tin (Sn) has been considered a promising alternative candidate for replacing lead in forming non-toxic perovskite materials. Nevertheless, the ease of oxidation of $Sn^{2+}$ to $Sn^{4+}$ presents a significant challenge to making ambient stable lead-free perovskite for practical applications.[10]

The lead-free double perovskite cesium silver bismuth bromide ($Cs_2AgBiBr_6$) has gained significant attention due to its favorable optoelectronic properties and crystal structure, closely resembling those of LHPs.[11] More importantly, $Cs_2AgBiBr_6$ exhibits excellent ambient stability and negligible toxicity,[12] making it an attractive candidate for various applications.[13] It has been extensively studied for use in solar cells, photodetectors, memristors, X-ray detectors, photocatalysis, and gas and humidity sensors.[14] In perovskite solar cells (PSCs), hydrogenated $Cs_2AgBiBr_6$-based light absorbers have achieved a record power conversion efficiency (PCE) of 6.37%.[11] In photodetectors, $Cs_2AgBiBr_6$ has demonstrated a high responsivity ($R$) of 54.6 A $W^{-1}$ and a specific detection rate ($D^*$) of $7.4 \times 10^{14}$ Jones.[13] Additionally, flexible and durable memristors using $Cs_2AgBiBr_6$ thin films have been

successfully fabricated, further demonstrating their potential for future optoelectronic applications.[15]

A key advantage of perovskite technology is its solution processability, enabling cost-effective and scalable coating or printing techniques for manufacturing. However, forming high-quality solution-processed $Cs_2AgBiBr_6$ films presents more significant challenges than LHPs.[16] It has been widely reported that solution-processed $Cs_2AgBiBr_6$ *via* the spin-coating process leads to poor film morphology with large agglomerates and excessive pinholes due to the rapid crystallization and high annealing temperature.[17–19] Therefore, it is essential to achieve high-quality $Cs_2AgBiBr_6$ films with dense morphology, smooth surfaces, large grain sizes, and minimal pinholes to optimize optoelectronic device performance.[16]

Antisolvent treatment is an effective strategy for regulating perovskite crystallization to achieve optimal film morphology. Zhao *et al.* used CB as an antisolvent during a one-step spin-coating process in a glovebox, resulting in the formation of dense and uniform $Cs_2AgBiBr_6$ films with a PCE of 1.33%.[20] Pantaler *et al.* also utilized CB as an antisolvent and achieved a PCE of 1.26% for PSCs.[21] Zeng *et al.* used methyl acetate (MA) as the antisolvent to obtain the high-quality $Cs_2AgBiBr_6$ film in the glovebox for memristors.[15] Gao *et al.* used isopropanol (IPA) as the antisolvent and achieved a PCE of 2.2% in their PSCs.[22] The antisolvent treatment can also be developed into a scalable bathing process that is compatible with the up-scaling printing process for industrial-scale and roll-to-roll manufacturing.[23,24]

Recently, Abdelsamie *et al.* employed *in situ* spectroscopy to investigate the formation of $Cs_2AgBiBr_6$ films using IPA as the antisolvent in the glovebox.[25] Their findings confirmed the critical role of antisolvents in improving film morphology. Additionally, they performed data mining across 56 publications to summarize the recent recipes for preparing $Cs_2AgBiBr_6$. Among these, CB is identified as the most commonly used antisolvent, appearing in 39% of cases (17% of the total studies with or without antisolvents), followed by IPA (10%), ethanol (7%), and toluene (5%). Furthermore, they noted that 88% of the studies on $Cs_2AgBiBr_6$ films were conducted in controlled environments such as gloveboxes or in conditions not specified, with only 12% in ambient conditions. The impact of different processing conditions (*e.g.* in ambient air or a glovebox) on the film morphology of $Cs_2AgBiBr_6$ still remains unclear. Most high-quality $Cs_2AgBiBr_6$ films for high-performance devices have been fabricated under controlled conditions within a glovebox.[20,25,26]

Nevertheless, developing ambient fabrication processes for high-quality $Cs_2AgBiBr_6$ films is crucial to reducing manufacturing costs and enabling industrial-scale printing and roll-to-roll manufacturing. For such an ambient process with antisolvent treatment, the careful selection of antisolvents and solvents is vital, not only to ensure film quality but also to mitigate health risks and align with environmental sustainability standards. Antisolvents such as chlorobenzene (CB) or toluene, used for $Cs_2AgBiBr_6$ film fabrication under ambient conditions, pose potential health and environmental risks due

to their low threshold limit values—the maximum airborne concentration permissible during an 8-hour workday without adverse health effects.[27,28] Green solvent and antisolvent strategies, guided by the CHEM21 framework, have been extensively studied for LHPs.[9] However, the research of green solvent engineering to $Cs_2AgBiBr_6$ films remains in its early stages, particularly for ambient processing. Advancing research in this area is essential to support the sustainable and scalable production of $Cs_2AgBiBr_6$-based devices.

In this study, we demonstrate an ambient fabrication process for producing high-quality $Cs_2AgBiBr_6$ films with dense and smooth morphology, even under relative humidity (RH) conditions of 60–70%. This process employs ethyl acetate (EA) as the antisolvent in a one-step deposition method. EA antisolvent treatment significantly improves the surface coverage, film morphology, and crystallinity of $Cs_2AgBiBr_6$ films, resulting in a high-quality film with minimal pinholes and defects compared to pristine films. Given that our method operates under ambient conditions, we also evaluated the toxicity of the antisolvent (EA) and solvent (dimethyl sulfoxide, DMSO) using the CHEM21 framework and compared it with recent studies. Both EA and DMSO are categorized as "recommended" solvents. Consequently, ambient-processed PSCs based on EA-treated films exhibit a five-fold increase in PCE compared to devices fabricated without EA treatment. This simple and glovebox-free processing strategy enables the fabrication of high-quality $Cs_2AgBiBr_6$ films under ambient air conditions. It broadens accessibility and supports the development of lead-free perovskite materials for various future optoelectronic applications such as solar cells, photodetectors, and memristors.

## 2. Results and discussion

As illustrated in Fig. 1a, we utilized a one-step spin coating process to deposit the $Cs_2AgBiBr_6$ film entirely in ambient air under an RH of 60–70% or in a glovebox under a low moisture level (~1 ppm) nitrogen atmosphere. The perovskite precursor solution was prepared by directly dissolving CsBr, $BiBr_3$, and AgBr salts in a molar ratio of 2 : 1 : 1 in the dimethyl sulfoxide (DMSO). After magnetic stirring the precursor solution at 70 for 1 hour, a homogeneous and clear precursor solution was obtained, as shown in Fig. S1 in ESI.† The fluorine-doped tin oxide (FTO) coated glass or indium tin oxide (ITO) substrates were preheated to 70 °C before the deposition of the precursor solution. Previous studies suggested that a preheating treatment can enhance the quality and surface coverage of the $Cs_2AgBiBr_6$ films.[17] The pristine $Cs_2AgBiBr_6$ film was prepared by directly spin-coating the precursor solution onto FTO- or ITO-glass substrates, followed by annealing at 280 °C for 5 minutes to complete the fabrication process. For the EA-treated film, an antisolvent technique was applied, as illustrated in Fig. 1b. In this method, EA was deposited during the spin-coating of the precursor solution, with subsequent procedures identical to those used for the pristine film. Detailed fabrication processes are provided in ESI.†

Fig. 1c displays actual images of the glovebox-processed and ambient-processed pristine and EA-treated $Cs_2AgBiBr_6$ films deposited on the FTO-glass substrates. The glovebox-processed pristine film demonstrated good film coverage with a uniform appearance. In contrast, the ambient-processed pristine film showed poor coverage, with visible holes and an island-like morphology. On the other hand, both the glovebox-
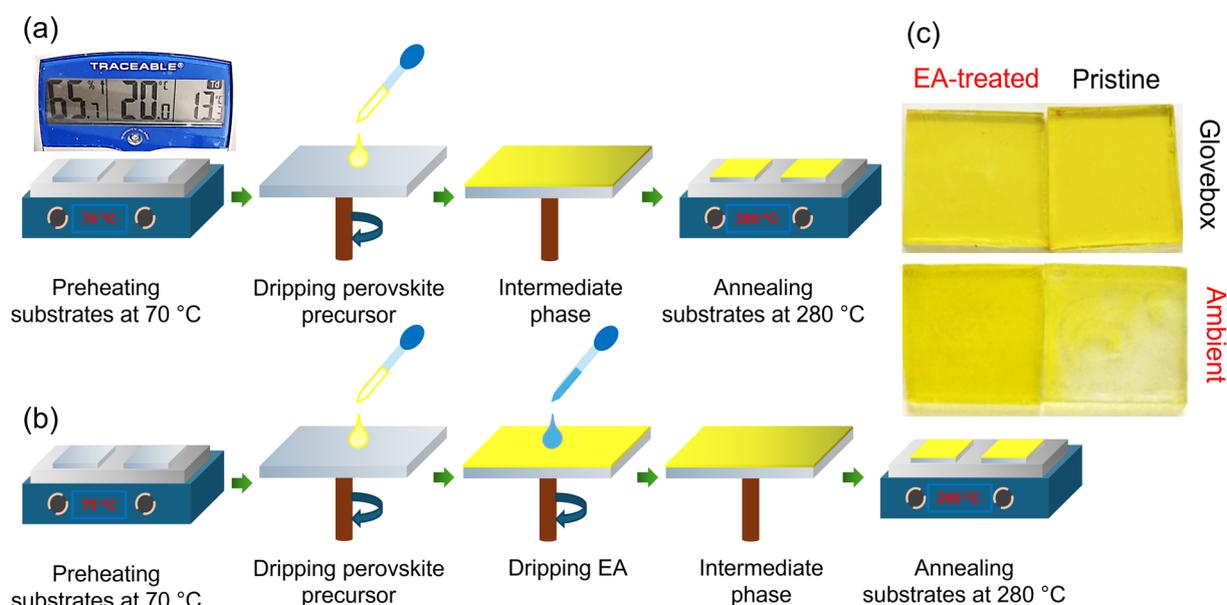


**Fig. 1** (a) Schematic illustration of the ambient process to fabricate pristine $Cs_2AgBiBr_6$ films with a humidity monitor showing an RH of 65.7% during the fabrication process. (b) Ambient process to fabricate EA-treated $Cs_2AgBiBr_6$ films. (c) Photographic images of actual pristine and EA-treated $Cs_2AgBiBr_6$ films coated on the FTO-glass fabricated in the ambient air and glovebox.
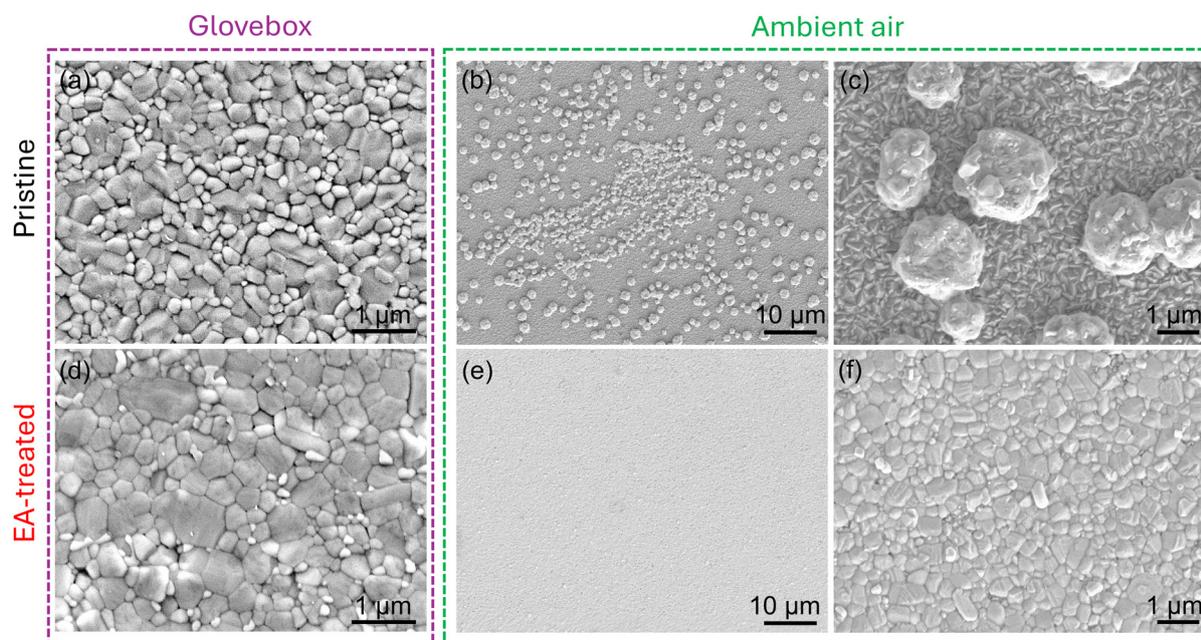
processed and ambient-processed EA-treated films showed a smooth and yellow surface with excellent film coverage on both FTO- and ITO-glass, as shown in Fig. 1c and S2 (ESI†). These results reveal the critical role of processing conditions and EA treatment in determining the surface coverage and quality of the $Cs_2AgBiBr_6$ films.

We then use field emission scanning electron microscopy (FEG-SEM) to further study the morphology of the pristine and EA-treated $Cs_2AgBiBr_6$ films prepared in both glove box and ambient air. As shown in Fig. 2a, the glovebox-processed pristine film showed a dense and smooth morphology. In contrast, the ambient-processed pristine films showed large agglomerates with a size of several μm that are loosely distributed on the substrate, as shown in Fig. 2b and c. Previous studies have attributed the formation of these large agglomerates to the rapid crystallization process induced by the high solvent evaporation rate during preheating treatment and the relatively high annealing temperature for obtaining the pure phase of $Cs_2AgBiBr_6$.[17,19] However, our results suggest that variations in moisture levels resulting from glove box (~1 ppm) and ambient air (RH of 60–70%) also play a significant role in influencing the quality of $Cs_2AgBiBr_6$ films.

Previous studies on LHP films have shown that the solvent evaporation rate during the spin-coating process plays a crucial role in determining film quality.[29] A fast evaporation rate promotes rapid supersaturation of the perovskite precursor solution, leading to accelerated nucleation and a higher density of nucleation sites. This results in improved film coverage and more uniform morphology.[30,31] In our study, DMSO was used as the precursor solvent for $Cs_2AgBiBr_6$. When pro-

cessed inside a nitrogen-filled glovebox with low humidity (approximately 1 ppm moisture), DMSO evaporated relatively quickly. This facilitated rapid supersaturation and nucleation, yielding a film with good coverage and uniformity, as shown in Fig. 2a. In contrast, under ambient conditions, DMSO tends to absorb moisture from the surrounding air due to its hygroscopic nature. The absorbed moisture slows down the evaporation rate of the solvent, which delays supersaturation and reduces the nucleation rate. According to the perovskite nucleation mechanism, this leads to a lower density of nucleation sites and a larger critical nucleus radius.[29] Upon annealing, these factors contribute to the growth of fewer but larger crystalline domains, resulting in an island-like film morphology with large particle features, as presented in Fig. 2b and c.

The glovebox-processed EA-treated film also showed a dense and smooth morphology, as shown in Fig. 2d. However, in contrast to the ambient-processed pristine film, the ambient-processed EA-treated film exhibited a dense and smooth morphology across various magnifications, as shown in Fig. 2e and f. As EA and DMSO are miscible, EA can effectively extract DMSO from the $Cs_2AgBiBr_6$ precursor solution during spin-coating. This rapid removal of the DMSO accelerates solvent evaporation, leading to quick supersaturation of the precursor. As a result, nucleation occurs rapidly with a high density of nucleation sites, which improves the uniformity and coverage of the resulting film. More importantly, EA possesses a significantly higher moisture absorption capacity compared to commonly used antisolvents such as toluene, CB, and diethyl ether.[32,33] During spin-coating in ambient con-



**Fig. 2** Top surface SEM images for the (a) glovebox-processed pristine films and ambient-processed pristine films under (b) low-magnification and (c) high-magnification. (d) Glovebox-processed EA-treated film and ambient-processed EA-treated films under (e) low-magnification and (f) high-magnification.

ditions, EA can absorb moisture both from the precursor solution and the surrounding air. This ability helps regulate the local microenvironment at the film surface in two ways: (1) it accelerates solvent evaporation by drawing moisture away from the ambient deposited precursor solution, enhancing supersaturation and promoting fast nucleation, and (2) it reduces the direct interaction between water molecules from ambient air and the forming perovskite nuclei during the spin-coating process, which otherwise could disrupt the crystallization process. Together, these effects contribute to a more controlled and uniform crystallization pathway. This ultimately results in the smooth and compact film morphology observed in Fig. 2e and f.

To investigate the film composition and elemental distribution of the ambient-processed pristine and EA-treated $Cs_2AgBiBr_6$ films, we performed SEM energy-dispersive X-ray (EDX) elemental mapping analysis on the film surfaces. As shown in Fig. 3a and S3 (ESI†), the ambient-processed pristine film showed large $Cs_2AgBiBr_6$ aggregates that were loosely distributed across the substrate. Elemental mapping (highlighted in pink) for indium (In) in Fig. 3b revealed large areas of uncoated ITO substrate. The EDX spectra in Fig. 3c further confirmed the poor surface coverage of the pristine film, as evidenced by strong In peaks (circled in red). This poor coverage is likely detrimental to device performance, as it can lead to severe charge recombination resulting from direct contact between different functional layers. In contrast, the EA-treated films demonstrated a uniform distribution of Cs, Ag, Bi, and Br across the film surface, as shown in Fig. 3d, e and Fig. S3 (ESI†), with minimal exposure of In, as confirmed by the EDX

spectra in Fig. 3f. The compact and uniform morphology of these films promotes efficient light absorption while suppressing charge recombination, thereby significantly enhancing the performance of devices such as PSCs and photodetectors.[34,35]

To investigate the film thickness, cross-sectional morphology, and composition of the ambient-processed pristine and EA-treated $Cs_2AgBiBr_6$ films, we performed cross-sectional SEM and EDX analyses. As shown in Fig. 4a–c, the ambient-processed pristine film exhibited isolated large aggregates with a maximum height reaching up to 710 nm, consistent with the surface SEM observations. In contrast, the ambient-processed EA-treated film displayed a relatively uniform and smooth morphology over a large area, as shown in Fig. 4d–g. This uniform cross-sectional structure is critical for light absorbers in PSCs, as it reduces the charge recombination sites and thereby enhances photovoltaic performance.[36,37] The average thickness of the ambient-processed EA-treated film was approximately 210 nm.

To investigate the crystallinity of the ambient-processed pristine and EA-treated $Cs_2AgBiBr_6$ films, we performed XRD analysis, as shown in Fig. 5. Lebail refinement of the XRD patterns was conducted using the FullProf Suite to fit the data to a simulated profile. The XRD patterns for both sample types were indexed to the cubic perovskite phase of $Cs_2AgBiBr_6$, with a space group of $Fm\bar{3}m$ and a unit cell parameter of 11.28 Å, in agreement with previous studies.[38,39] The EA-treated film exhibited significantly stronger relative intensities for the XRD peaks corresponding to $Cs_2AgBiBr_6$ compared to the pristine film, while maintaining similar full width at half maximum
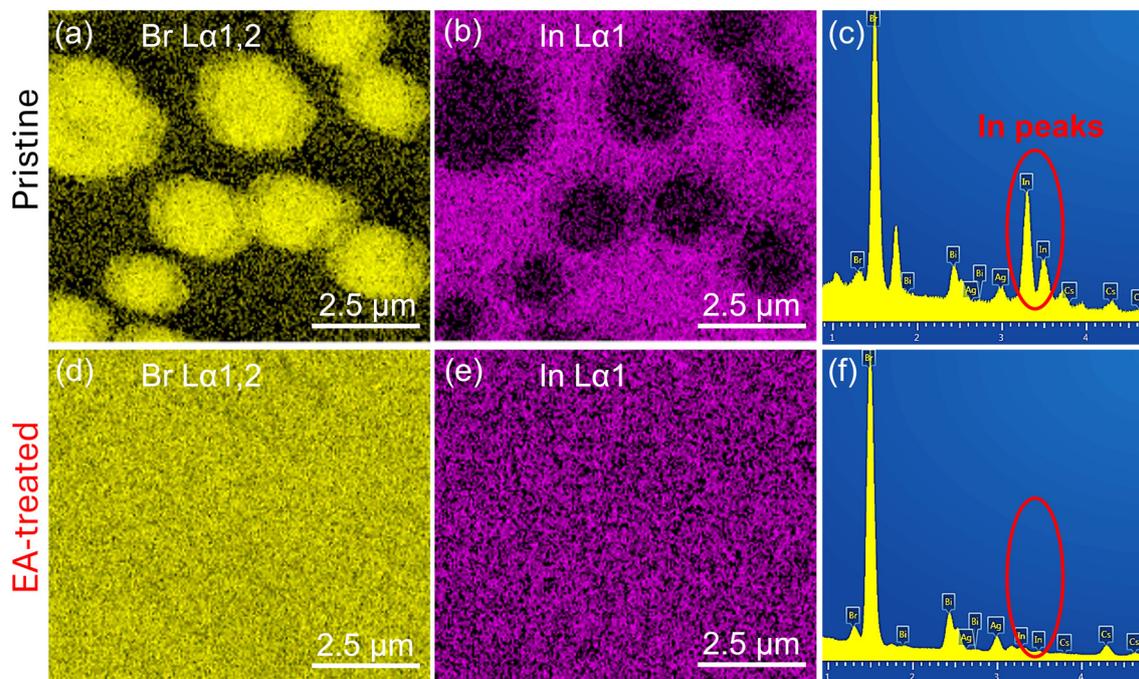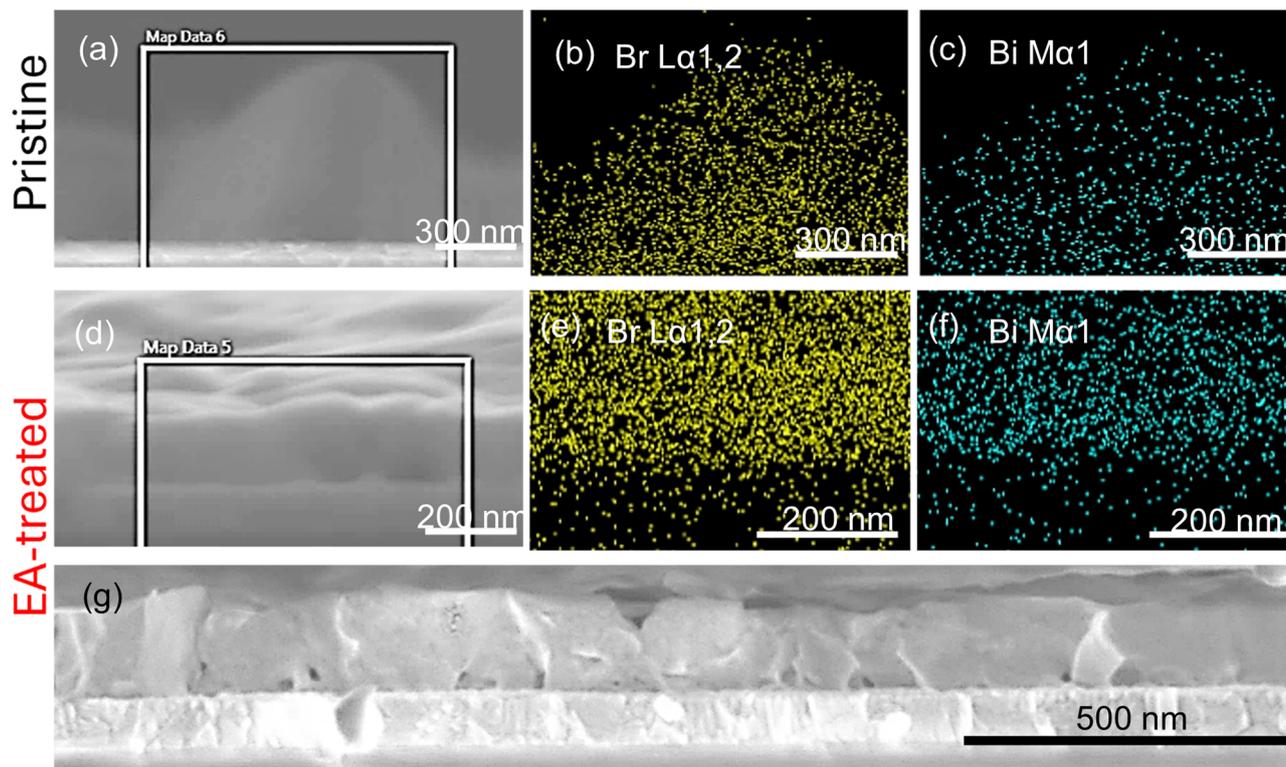


**Fig. 3** Top surface EDX elemental mapping of (a) Br and (b) In for the ambient-processed pristine film, (d) Br and (e) In for the ambient-processed EA-treated film. EDX spectrum for ambient-processed (c) pristine and (f) EA-treated films.

**Fig. 4** (a) Cross-sectional SEM for the pristine film, and its corresponding EDX for (b) Br and (c) Bi elemental distribution. (d) Cross-sectional SEM for the EA-treated film, and its corresponding EDX for (e) Br and (f) Bi elemental distribution. (g) Cross-sectional SEM imaging of the EA-treated film over an extended area.

(FWHM) values, as summarized in Table S1 (ESI†). This indicates improved crystallinity of the antisolvent-treated $Cs_2AgBiBr_6$ films relative to the pristine samples, consistent with the SEM results. A minor impurity phase of $Cs_3Bi_2Br_9$ was detected in both the pristine and EA-treated film, possibly due to annealing the $Cs_2AgBiBr_6$ films in ambient air above 250 °C.[40]

X-ray photoelectron spectroscopy (XPS) is a powerful tool for analyzing the surface chemistry of thin-film materials.[41] We conducted the XPS analysis to probe the surface chemistry of the ambient-processed pristine and EA-treated $Cs_2AgBiBr_6$ films. As shown in Fig. 6a, the XPS survey spectra confirm the presence of Cs, Ag, Bi, Br, silicon (Si), and oxygen (O) elements. The atomic concentrations of these elements are summarized in Fig. S4.† Notably, the relative atomic concentrations of Si and O were significantly higher in the ambient-processed pristine film (41.7 at% and 44.9 at%, respectively) compared to the EA-treated film (23.57 at% and 35.3 at%, respectively). This elevated Si and O content in the pristine film is attributed to its poor surface coverage, which leaves substantial portions of the underlying quartz glass substrate exposed. In contrast, the EA-treated film exhibits enhanced surface coverage, effectively reducing substrate exposure and lowering oxygen content, consistent with SEM and EDX findings. High-resolution XPS spectra for Cs 3d, Ag 3d, Bi 4f, and Br 3d are presented in Fig. 6b–d and Fig. S5 (ESI†). The peak

positions corresponding to Cs $3d_{3/2}$, Cs $3d_{5/2}$, Ag $3d_{3/2}$, Ag $3d_{5/2}$, Bi $4f_{5/2}$, Bi $4f_{7/2}$, Br $3d_{3/2}$ and Br $3d_{5/2}$ in both ambient-processed pristine and EA-treated films are summarized in Table S2 (ESI†), showing good agreement with previous studies.[42,43] No significant peak shifts were observed between the ambient-processed pristine and EA-treated $Cs_2AgBiBr_6$ films.

To examine the optical properties of the ambient-processed pristine and EA-treated $Cs_2AgBiBr_6$ films, we performed the ultraviolet-visible-near-infrared (UV-vis-NIR) spectroscopy. As shown in Fig. 7a, the EA-treated film exhibits an absorption peak at 438 nm and an absorption edge around 600 nm, consistent with previous studies on high-quality $Cs_2AgBiBr_6$ films.[18] In contrast, the pristine film demonstrates significantly lower absorption. This is attributed to the poor surface coverage with large uncovered areas, as evident from Fig. 1c and Fig. S2 (ESI†). Given that $Cs_2AgBiBr_6$ is considered an indirect semiconductor, its Tauc plot was constructed using the equation:

$$(\alpha h\nu)^{1/2} = A (h\nu - E_g) \tag{1}$$

where $A$ is a proportionality constant, $\alpha$ is the absorption coefficient, $h$ is Planck's constant, $\nu$ is the frequency of the incident light. From the Tauc plot shown inset to Fig. 7a, the bandgap of the EA-treated $Cs_2AgBiBr_6$ films was determined to
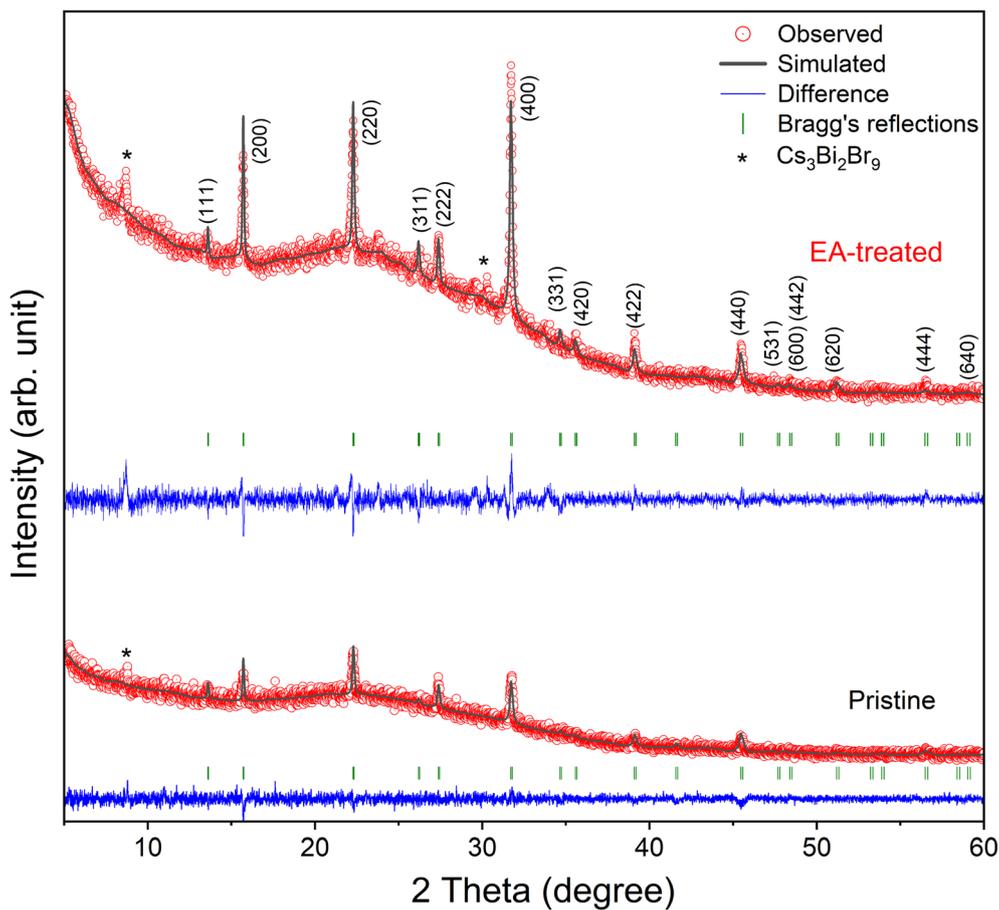
**Fig. 5** XRD patterns for the ambient-processed EA-treated (top) and pristine (bottom) $Cs_2AgBiBr_6$ films.

be 2.15 eV, consistent with previous reports indicating a range of 2.1–2.3 eV.[44] In contrast, determining the bandgap for the ambient-processed pristine film using a Tauc plot was challenging due to its poor absorbance, as shown in Fig. S6 (ESI†).

To further explore the optical properties, steady-state photoluminescence (PL) spectroscopy was conducted as shown in Fig. 7b. Since both the pristine and EA-treated films were deposited onto quartz glass for PL measurements, the significantly enhanced PL intensity observed in the EA-treated films suggests a notable improvement in spontaneous radiative recombination with a higher generation of free charge carriers and suppressed non-radiative recombination. We attribute this enhancement to three main factors. First, the EA-treated film exhibits improved light absorption, as confirmed by UV-vis-NIR results. This is due to their enhanced surface coverage and film morphology compared to pristine film, as evidenced by SEM surface analysis. Second, unlike the pristine films, which contain large aggregates, the EA-treated films are more compact and uniform, reducing the density of pinholes and grain boundaries that commonly serve as non-radiative recombination centres.[45] SEM cross-sectional analysis also reveals a smoother interface between the EA-treated film and the substrate, further minimizing interface recombination losses.[46]

Third, XRD analysis exhibits enhanced crystallinity for EA-treated film, which facilitates charge carrier transport and suppresses defect-mediated recombination. We believe these combined effects lead to the significantly enhanced PL intensity observed in the EA-treated films.

To evaluate the photovoltaic performance of the ambient-processed pristine and EA-treated $Cs_2AgBiBr_6$ films, we assembled the PSCs with an architecture of ITO-glass/compact and mesoporous $TiO_2$/$Cs_2AgBiBr_6$/spiro-OMeTAD/Au, as illustrated in Fig. 8a. Except for the thermal evaporation of the Au electrode, the entire device fabrication process was carried out in ambient air with an RH of 60–70%. Fig. 8b shows the current density–voltage ($J$–$V$) curves under AM1.5 sunlight and dark conditions for the champion cells based on the pristine and EA-treated films. The champion cell based on the EA-treated film achieved a champion PCE of 1.08%, representing a more than five-fold improvement compared to the pristine film-based PSCs, which achieved a champion PCE of 0.21%. The PCE for the PSCs based on the EA-treated $Cs_2AgBiBr_6$ films is comparable to several devices fabricated in inert glovebox environments with chlorobenzene or IPA as the antisolvents, as reported in recent literature.[20,47] The distribution and summary of photovoltaic parameters measured across multiple
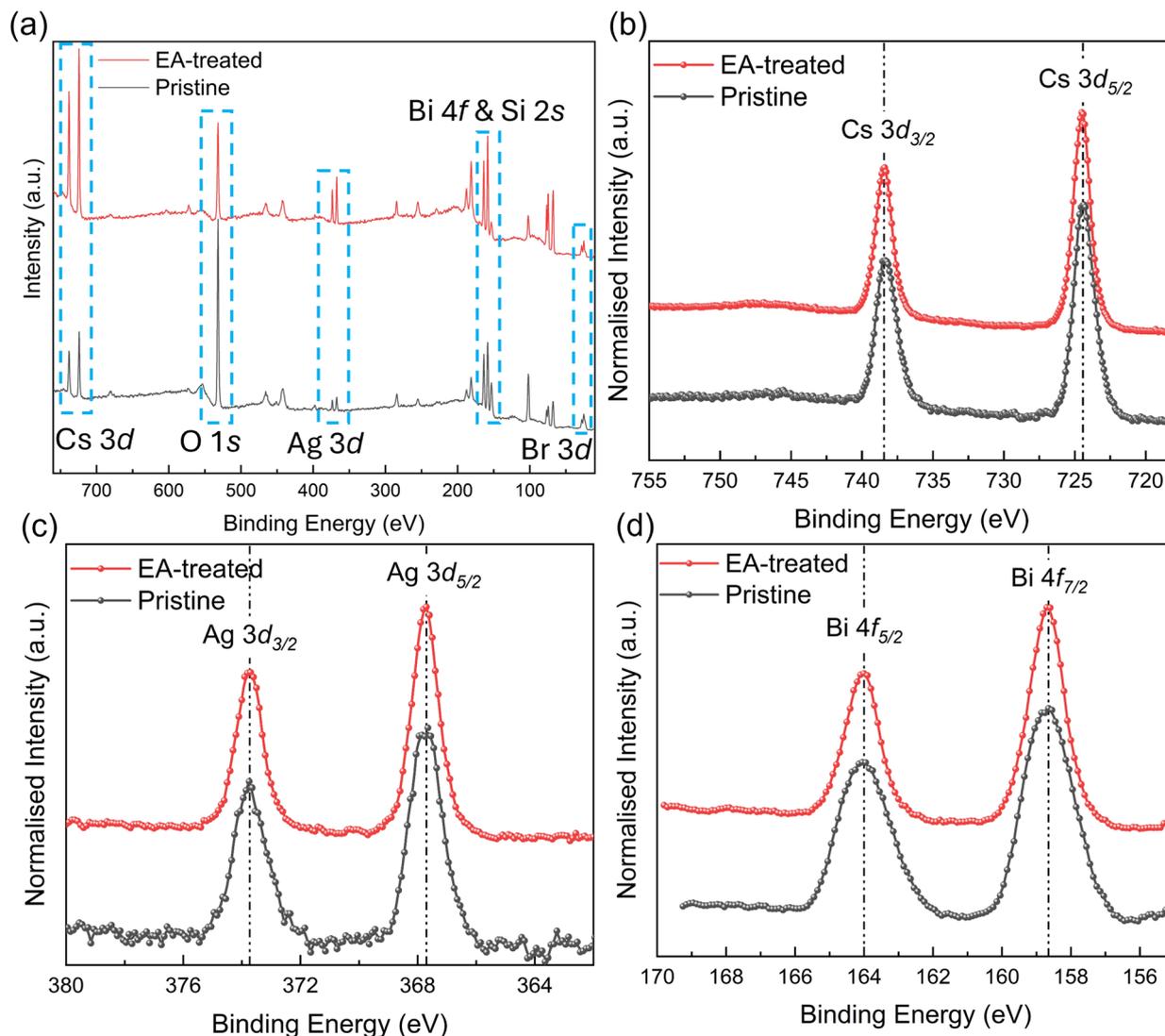
**Fig. 6** (a) XPS survey spectra for the ambient-processed pristine and EA-treated $Cs_2AgBiBr_6$ films. High-resolution XPS spectra of the element (b) Cs 3d, (c) Ag 3d, and (d) Bi 4f for the ambient-processed pristine and EA-treated $Cs_2AgBiBr_6$ films.

cells for both pristine and EA-treated films are presented in Fig. 8a, b, S7 (ESI), and Table S3 (ESI).† The improved PCE of the PSCs based on the EA-treated films is primarily attributed to the significantly higher short-circuit current density ($J_{SC}$) compared to the PSCs based on the pristine films. This enhancement arises from the dense and uniform morphology of the EA-treated film, which facilitates improved light absorption, as evidenced by UV-vis-NIR, PL, and SEM analyses. Furthermore, PSCs based on pristine films exhibited lower open-circuit voltages ($V_{OC}$) than those based on EA-treated films. This is due to poor surface coverage and the presence of large aggregates in the pristine film, which lead to direct contact between the electron transport layer ($TiO_2$) and the hole transport layer (spiro-OMeTAD), resulting in increased charge recombination. Additionally, PSCs fabricated with EA-treated films demonstrated relatively stable performance under varying scan rates and scan cycles, as shown in Fig. S8

(ESI†). The forward and reverse $J$–$V$ scans for the EA-treated PSCs are presented in Fig. S9 (ESI†).

Sustainable and cost-effective approaches are essential for developing new materials processing methods while minimizing environmental impact.[48,49] Beyond achieving a high-quality $Cs_2AgBiBr_6$ film, it is essential to consider the toxicity of the solvents and antisolvents used during fabrication, as well as the complexity of the fabrication process, particularly for ambient processing and industrial-scale production. Here, we summarize recent studies on the preparation of $Cs_2AgBiBr_6$ films using various methods, comparing them with our approach, as shown in Table 1. The CHEM21 solvent guide is a widely used tool for assessing the environmental sustainability of solvents and antisolvents used to fabricate perovskite films and devices.[9,50,51] Herein, the toxicity and environmental impact of solvents and antisolvents employed in recent studies on the fabrication of $Cs_2AgBiBr_6$ were assessed using the
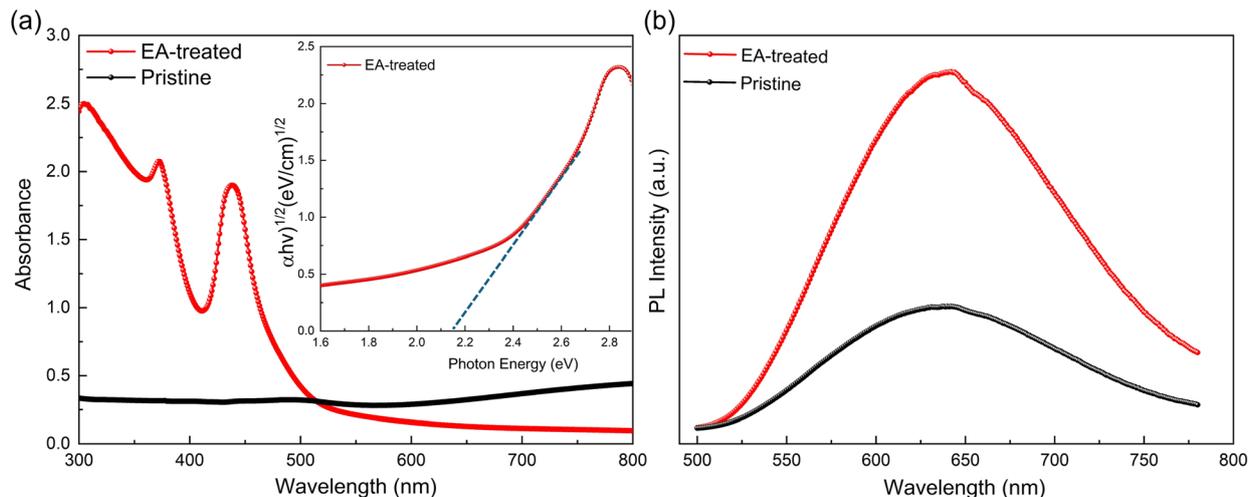
**Fig. 7** (a) Absorption spectra measured by UV-vis-NIR spectroscopy for the ambient-processed pristine and EA-treated $Cs_2AgBiBr_6$ films. Inset: Tauc plot of the indirect bandgap ambient-processed EA-treated $Cs_2AgBiBr_6$ films. (b) Steady-state PL spectra for the ambient-processed pristine and EA-treated $Cs_2AgBiBr_6$ films.
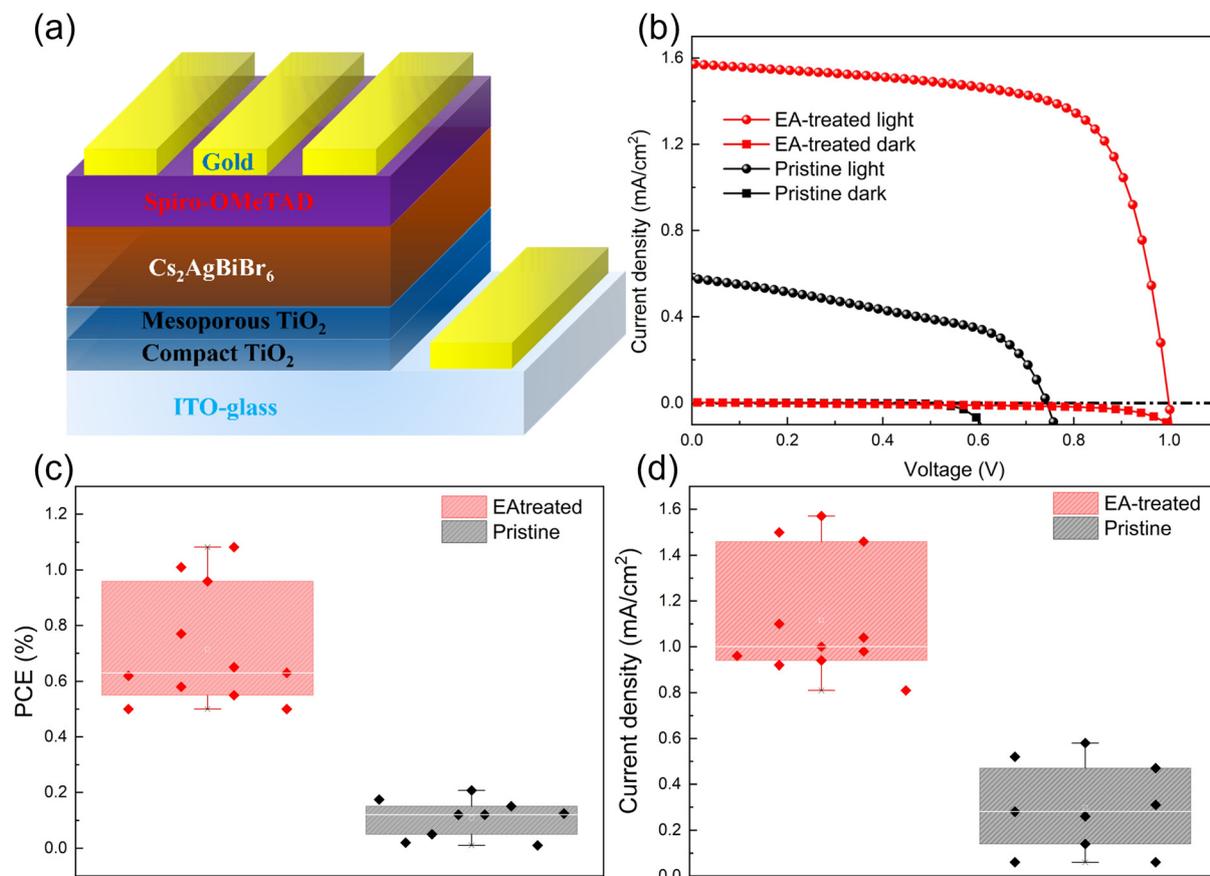


**Fig. 8** (a) Schematic representation of PSCs based on ITO-glass/compact and mesoporous $TiO_2$/$Cs_2AgBiBr_6$/spiro-OMeTAD/Au architecture. (b) $J$–$V$ curves under AM1.5 sunlight and dark for champion cells based on the ambient-processed pristine and EA-treated films. (c) PCE and (d) $J_{SC}$ distribution for the PSCs based on the ambient-processed pristine and EA-treated films.

**Table 1** A summary of processing conditions, precursor preparation method, film morphology, solvent, and antisolvent toxicity based on the CHEM21 solvent guide for recent studies on preparing $Cs_2AgBiBr_6$ films in comparison to our method

| Processing conditions | Precursor preparation | Solvent | Antisolvent | Film morphology | Ref. |
|---|---|---|---|---|---|
| **Ambient RH ≈ 60–70%** | **Direct dissolution** | **DMSO (R)** | **EA (R)** | **Smooth** | **This work** |
| Unspecified | Polycrystal powder | DMSO (R) | CB (P) | Smooth | 21 |
| Glovebox | Direct dissolution | DMF (H) DMSO (R) | CB (P) | Smooth | 20 |
| Glovebox | Direct dissolution | DMF (H) DMSO (R) | CB (P) | Smooth | 52 |
| Unspecified | Polycrystal powder | DMSO (R) | IPA (R) | Smooth | 22 |
| Glovebox | Direct dissolution | DMSO (R) | IPA (R) | Smooth | 11 |
| Glovebox | Direct dissolution | DMSO (R) | IPA (R) | Smooth | 47 |
| Glovebox | Direct dissolution | DMSO (R) | MA (P) | Smooth | 15 |
| Glovebox | Single crystal powder | DMSO (R) | — | Smooth | 56 |
| Ambient unspecified RH% | Direct dissolution | DMSO (R) | — | Aggregates | 17 |
| Ambient unspecified RH% | Direct dissolution | DMSO (R) | — | Aggregates | 57 |
| Ambient RH ≈ 50% | Polycrystal powder | DMSO (R) | — | Aggregates | 18 |
| Ambient RH ≈ 50% low-pressure annealing | Polycrystal powder | DMSO (R) | — | Smooth | 18 |

CHEM21 framework, which scores solvents based on safety, health, and environmental (SHE) criteria. These scores consider key physical properties and hazard statements, as summarized in Table S4 (ESI†). Based on the combined SHE scores, solvents and antisolvents were categorized into three levels: recommended (R), problematic (P), and hazardous (H). In our work, DMSO was used as the precursor solvent and EA as the antisolvent, both of which have an overall rating of R. By contrast, some studies have employed a 1:1 mixture of DMF and DMSO as the precursor solvent.[20,52] However, DMF is classified as H due to its high health score of 9, due to its high risk to human health through inhalation or skin exposure.[9] CB, another commonly used antisolvent, is categorized as P because of its high environmental score of 7, due to its ozone-depleting potential and water pollution risk.[53] IPA is another widely used antisolvent for $Cs_2AgBiBr_6$ films with a rating of R. However, most studies utilizing IPA have been performed in glove boxes, leaving its suitability for ambient processing unclear. Notably, MA has recently been used as an antisolvent for preparing $Cs_2AgBiBr_6$ films in the glovebox. While MA shares a similar chemical structure with EA, previous studies on using MA as the antisolvent for LHPs also suggested that MA has a higher water solubility than EA for the ambient processing of LHPs.[54] However, MA is categorized as P due to its higher environmental score and lower boiling point (57–58 °C) compared to EA (76.5–77.5 °C).[55] A lower boiling point increases the possibility of harmful volatile organic compound emissions. The ideal boiling point range for antisolvents is typically between 70 and 139 °C.[27]

We also compared the precursor preparation methods and resulting film morphologies achieved using different approaches under various processing conditions. A number of existing studies on high-quality $Cs_2AgBiBr_6$ film fabrication require the prior synthesis of $Cs_2AgBiBr_6$ crystalline powders, which are then dissolved in a solvent to prepare the perovskite precursor. For example, Pantaler et al. synthesized $Cs_2AgBiBr_6$ crystalline powder by dissolving CsBr, AgBr, and $BiBr_3$ salts in HBr at 150 °C for 2 hours, followed by cooling to room temp-

erature.[21] The resulting orange powder was then washed with ethanol and dried overnight, yielding 59.7%, and subsequently dissolved in DMSO for spin-coating the films, using CB as the antisolvent. These requirements increase manufacturing costs and lead times, making the process less sustainable and cost-effective for practical production. In contrast, our method employs a direct dissolution approach, eliminating the need for an intermediate crystallization step. By removing this process, our approach effectively reduces chemical and energy consumption as well as processing time. Moreover, by integrating a green antisolvent EA, our method offers a greener, more efficient, and sustainable approach for $Cs_2AgBiBr_6$ film fabrication. Additionally, as shown in Table 1, multiple studies on $Cs_2AgBiBr_6$ film fabrication report the formation of aggregates, highlighting the challenge of achieving uniform and compact films. The antisolvent technique we developed addresses this issue by enabling the production of high-quality $Cs_2AgBiBr_6$ films with smooth and dense morphologies under high relative humidity (RH) conditions of 60–70%. This reduces the dependence on expensive facilities such as glove boxes and humidity-controlled equipment, further reducing production costs and enhancing scalability.

## 3. Conclusion

In conclusion, we investigated the impact of processing conditions on the quality of $Cs_2AgBiBr_6$ films by comparing fabrication in ambient air and a nitrogen glovebox environment. This revealed the significant challenge of producing high-quality $Cs_2AgBiBr_6$ films under a high moisture level in ambient air. To overcome this challenge, we successfully demonstrated EA antisolvent treatment to fabricate dense and uniform $Cs_2AgBiBr_6$ films in ambient air, even under an RH of 60–70%. This approach led to a substantial improvement in film morphology and photovoltaic performance, with ambient-processed PSCs based on EA-treated films achieving a PCE of 1.08%, compared to 0.21% for pristine films. We believe this is

due to the high water solubility of EA that can withdraw moisture from the precursor solution and facilitate supersaturation that promotes the formation of dense and uniform films. Additionally, we evaluated the environmental impact of the solvents and antisolvents used in this study through the CHEM21 framework. Both EA as the antisolvent and DMSO as the precursor solvent received a "recommended" rating, highlighting their suitability for green and sustainable fabrication of $Cs_2AgBiBr_6$ films. Our findings demonstrate a cost-effective, sustainable, and environmentally friendly strategy for producing high-quality, non-toxic double perovskite $Cs_2AgBiBr_6$ films, offering promising potential for future optoelectronic applications.

## Data availability

The data supporting this article have been included as part of the ESI.† Additional data are available from the authors upon request.

## Conflicts of interest

There are no conflicts to declare.

## Acknowledgements

## References

1 J. Min, Y. Choi, D. Kim and T. Park, *Adv. Energy Mater.*, 2024, **14**, 2302659.

2 Y. Rong, Y. Hu, A. Mei, H. Tan, M. I. Saidaminov, S. Il Seok, M. D. McGehee, E. H. Sargent and H. Han, *Science*, 2018, **361**, eaat8235.

3 Y. Zhao and K. Zhu, *Chem. Soc. Rev.*, 2016, **45**, 655–689.

4 Z. Li, A. Johnston, M. Wei, M. I. Saidaminov, J. M. de Pina, X. Zheng, J. Liu, Y. Liu, O. M. Bakr and E. H. Sargent, *Joule*, 2020, **4**, 631–643.

5 NREL, Best Research-Cell Efficiencies chart, https://www.nrel.gov/pv/cell-efficiency.html.

6 M. Ren, X. Qian, Y. Chen, T. Wang and Y. Zhao, *J. Hazard. Mater.*, 2022, **426**, 127848.

7 J. Li, H.-L. Cao, W.-B. Jiao, Q. Wang, M. Wei, I. Cantone, J. Lü and A. Abate, *Nat. Commun.*, 2020, **11**, 310.

8 N. Moody, S. Sesena, D. W. deQuilettes, B. D. Dou, R. Swartwout, J. T. Buchman, A. Johnson, U. Eze, R. Brenes, M. Johnston, C. L. Haynes, V. Bulović and M. G. Bawendi, *Joule*, 2020, **4**, 970–974.

9 H. J. Kim, Y. J. Kim, G. S. Han and H. S. Jung, *Sol. RRL*, 2024, **8**, 2300910.

10 L. H. Hernandez, L. Lanzetta, S. Jang, J. Troughton, M. A. Haque and D. Baran, *ACS Energy Lett.*, 2023, **8**, 259–273.

11 Z. Zhang, Q. Sun, Y. Lu, F. Lu, X. Mu, S.-H. Wei and M. Sui, *Nat. Commun.*, 2022, **13**, 3397.

12 M. Zhai, C. Chen and M. Cheng, *Sol. Energy*, 2023, **253**, 563–583.

13 H. Lei, D. Hardy and F. Gao, *Adv. Funct. Mater.*, 2021, **31**, 2105898.

14 S. C. Yadav, A. Srivastava, V. Manjunath, A. Kanwade, R. S. Devan and P. M. Shirage, *Mater. Today Phys.*, 2022, **26**, 100731.

15 F. Zeng, Y. Tan, W. Hu, X. Tang, H. Yin, T. Jing, L. Huang, Y. Yang, J. Liao and C. Zhou, *Appl. Phys. Lett.*, 2024, **124**, 162101.

16 J. Huang, H. Xiang, R. Ran, W. Zhou, W. Wang and Z. Shao, *Renewable Sustainable Energy Rev.*, 2024, **191**, 114187.

17 E. Greul, M. L. Petrus, A. Binek, P. Docampo and T. Bein, *J. Mater. Chem. A*, 2017, **5**, 19972–19981.

18 C. Wu, Q. Zhang, Y. Liu, W. Luo, X. Guo, Z. Huang, H. Ting, W. Sun, X. Zhong, S. Wei, S. Wang, Z. Chen and L. Xiao, *Adv. Sci.*, 2018, **5**, 1700759.

19 M. S. Shadabroo, H. Abdizadeh and M. R. Golobostanfard, *ACS Appl. Energy Mater.*, 2021, **4**, 6797–6805.

20 D. Zhao, C. Liang, B. Wang, T. Liu, Q. Wei, K. Wang, H. Gu, S. Wang, S. Mei and G. Xing, *Energy Environ. Mater.*, 2022, **5**, 1317–1322.

21 M. Pantaler, K. T. Cho, V. I. E. Queloz, I. García-Benito, C. Fettkenhauer, I. Anusca, M. K. Nazeeruddin, D. C. Lupascu and G. Grancini, *ACS Energy Lett.*, 2018, **3**, 1781–1786.

22 W. Gao, C. Ran, J. Xi, B. Jiao, W. Zhang, M. Wu, X. Hou and Z. Wu, *ChemPhysChem*, 2018, **19**, 1696–1700.

23 D. S. Ham, W. J. Choi, H. Yun, M. Kim, D.-H. Yeo, S. Lee, B. J. Kim and J. H. Lee, *ACS Appl. Energy Mater.*, 2021, **4**, 7611–7621.

24 Y. Y. Kim, T.-Y. Yang, R. Suhonen, A. Kemppainen, K. Hwang, N. J. Jeon and J. Seo, *Nat. Commun.*, 2020, **11**, 5146.

25 M. Abdelsamie, K. Cruse, N. Tamura, G. Ceder and C. M. Sutter-Fella, *J. Mater. Chem. A*, 2022, **10**, 19868–19880.

26 T. Luo, Y. Zhang, X. Chang, J. Fang, T. Niu, J. Lu, Y. Fan, Z. Ding, K. Zhao and S. (Frank) Liu, *J. Energy Chem.*, 2021, **53**, 372–378.

27 D. Prat, A. Wells, J. Hayler, H. Sneddon, C. R. McElroy, S. Abou-Shehada and P. J. Dunn, *Green Chem.*, 2016, **18**, 288–296.

28 Q. Chen, J. C. R. Ke, D. Wang, M. Z. Mokhtar, A. G. Thomas and Z. Liu, *Appl. Surf. Sci.*, 2021, **536**, 147949.

29 H. Gao, C. Bao, F. Li, T. Yu, J. Yang, W. Zhu, X. Zhou, G. Fu and Z. Zou, *ACS Appl. Mater. Interfaces*, 2015, **7**, 9110–9117.

30 S. Sánchez, L. Pfeifer, N. Vlachopoulos and A. Hagfeldt, *Chem. Soc. Rev.*, 2021, **50**, 7108–7131.

31 G. Wang, D. Liu, J. Xiang, D. Zhou, K. Alameh, B. Ding and Q. Song, *RSC Adv.*, 2016, **6**, 43299–43303.

32 J. Troughton, K. Hooper and T. M. Watson, *Nano Energy*, 2017, **39**, 60–68.

33 Q. Chen, M. Z. Mokhtar, J. C.-R. Ke, A. G. Thomas, A. Hadi, E. Whittaker, M. Curioni and Z. Liu, *Sustainable Energy Fuels*, 2018, **2**, 1216–1224.

34 D. Shen, X. Yu, X. Cai, M. Peng, Y. Ma, X. Su, L. Xiao and D. Zou, *J. Mater. Chem. A*, 2014, **2**, 20454–20461.

35 W. Shen, U. Jung, Z. Xian, B. Jung and J. Park, *J. Alloys Compd.*, 2022, **929**, 167329.

36 P. Jia, L. Qin, D. Zhao, Y. Tang, B. Song, J. Guo, X. Li, L. Li, Q. Cui, Y. Hu, Z. Lou, F. Teng and Y. Hou, *Adv. Funct. Mater.*, 2021, **31**, 2107125.

37 S. Takahashi, S. Uchida, P. V. V. Jayaweera, S. Kaneko and H. Segawa, *Sci. Rep.*, 2023, **13**, 16068.

38 N. K. Tailor, N. Parikh, P. Yadav and S. Satapathi, *J. Phys. Chem. C*, 2022, **126**, 10199–10208.

39 W. Yuan, G. Niu, Y. Xian, H. Wu, H. Wang, H. Yin, P. Liu, W. Li and J. Fan, *Adv. Funct. Mater.*, 2019, **29**, 1900234.

40 P. Pistor, M. Meyns, M. Guc, H.-C. Wang, M. A. L. Marques, X. Alcobé, A. Cabot and V. Izquierdo-Roca, *Scr. Mater.*, 2020, **184**, 24–29.

41 X. Wu, Q. Yan, H. Wang, D. Wu, H. Zhou, H. Li, S. Yang, T. Ma and H. Zhang, *Adv. Funct. Mater.*, 2024, **34**, 2404535.

42 G. Yan, B. Jiang, Y. Yuan, M. Kuang, X. Liu, Z. Zeng, C. Zhao, J.-H. He and W. Mai, *ACS Appl. Mater. Interfaces*, 2020, **12**, 6064–6073.

43 F. Igbari, R. Wang, Z.-K. Wang, X.-J. Ma, Q. Wang, K.-L. Wang, Y. Zhang, L.-S. Liao and Y. Yang, *Nano Lett.*, 2019, **19**, 2066–2073.

44 Z. Li, S. R. Kavanagh, M. Napari, R. G. Palgrave, M. Abdi-Jalebi, Z. Andaji-Garmaroudi, D. W. Davies, M. Laitinen, J. Julin, M. A. Isaacs, R. H. Friend, D. O. Scanlon, A. Walsh and R. L. Z. Hoye, *J. Mater. Chem. A*, 2020, **8**, 21780–21788.

45 J. Tao, C. Zhao, Z. Wang, Y. Chen, L. Zang, G. Yang, Y. Bai and J. Chu, *Energy Environ. Sci.*, 2025, **18**, 509–544.

46 C. M. Wolff, P. Caprioglio, M. Stolterfoht and D. Neher, *Adv. Mater.*, 2019, **31**, 1902762.

47 M. T. Sirtl, M. Armer, L. K. Reb, R. Hooijer, P. Dörflinger, M. A. Scheel, K. Tvingstedt, P. Rieder, N. Glück, P. Pandit, S. V. Roth, P. Müller-Buschbaum, V. Dyakonov and T. Bein, *ACS Appl. Energy Mater.*, 2020, **3**, 11597–11609.

48 Y. Zhou, Y. Zhang, Y. Nie, D. Sun, D. Wu, L. Ban, H. Zhang, S. Yang, J. Chen, H. Du and X. Pan, *Prog. Mater. Sci.*, 2025, **152**, 101460.

49 Y. Nie, Y. Zhou, Y. Zhang, D. Sun, D. Wu, L. Ban, S. Nanda, C. Xu and H. Zhang, *Adv. Funct. Mater.*, 2025, 2418957, DOI: **10.1002/adfm.202418957**.

50 C. Duan, H. Gao, K. Xiao, V. Yeddu, B. Wang, R. Lin, H. Sun, P. Wu, Y. Ahmed, A. D. Bui, X. Zheng, Y. Wang, J. Wen, Y. Wang, W. Ou, C. Liu, Y. Zhang, H. Nguyen, H. Luo, L. Li, Y. Liu, X. Luo, M. I. Saidaminov and H. Tan, *Nat. Energy*, 2025, **10**, 318–328.

51 F. Meng, L. Cheng, F. Wang, K. Chen, Z. Sun and G. Wang, *Adv. Sustainable Syst.*, 2025, **9**, 2400695.

52 D. Zhao, B. Wang, C. Liang, T. Liu, Q. Wei, S. Wang, K. Wang, Z. Zhang, X. Li, S. Peng and G. Xing, *Sci. China Mater.*, 2020, **63**, 1518–1525.

53 S. K. Podapangi, F. Jafarzadeh, S. Mattiello, T. B. Korukonda, A. Singh, L. Beverina and T. M. Brown, *RSC Adv.*, 2023, **13**, 18165–18206.

54 F. Yang, G. Kapil, P. Zhang, Z. Hu, M. A. Kamarudin, T. Ma and S. Hayase, *ACS Appl. Mater. Interfaces*, 2018, **10**, 16482–16489.

55 N. A. Mali, S. S. Yadav, P. D. Ghuge and S. S. Joshi, *J. Chem. Eng. Data*, 2017, **62**, 4356–4363.

56 W. Ning, F. Wang, B. Wu, J. Lu, Z. Yan, X. Liu, Y. Tao, J.-M. Liu, W. Huang, M. Fahlman, L. Hultman, T. C. Sum and F. Gao, *Adv. Mater.*, 2018, **30**, 1706246.

57 B. Kumaar Swamy Reddy, A. S. Kumar, R. Akash, E. Ramasamy, S. Badhulika, G. Veerappan and P. H. Borse, *Sol. Energy*, 2024, **283**, 112989.